Carbon monoxide emissions at 4.7 micrometres from Venus' atmosphere*

Jacques Crovisier[a]†, Emmanuel Lellouch[a], Catherine de Bergh[a], Jean-Pierre Maillard[b], Barry L. Lutz[c], Bruno Bézard[a]

April 28, 2006

[a] LESIA, Observatoire de Paris, 5 place Jules Janssen, F–92195 Meudon, France
[b] Institut d'Astrophysique de Paris, 98bis boulevard Arago, F–75014 Paris, France
[c] Northern Arizona University, Flagstaff, AZ 86011–6010, USA

Abstract

In January 1987, high-resolution spectra of the dayside of Venus in the 2080–2185 cm^{-1} range, recorded with the Canada–France–Hawaii telescope using a Fourier-transform spectrometer, revealed two sequences of narrow emission lines, corresponding to the v = (1–0) and v = (2–1) vibrational bands of carbon monoxide. Higher-quality spectra of Venus were recorded subsequently (September 1994) on several points on Venus. We present here the Venus observations and the associated intensities and rotational temperatures. Possible mechanisms responsible for these emissions are reviewed. We show that (1) fluorescence following infrared solar excitation and (2) CO_2 photolysis leading to the creation of vibrationally excited CO are two plausible mechanisms. A quantitative model which takes into account these two processes, collisions and radiative trapping is presented and allows an approximate matching of the observed line intensities. Inferred temperatures are 170–220 K for the (2–1) band, probing the 100–110 km range, and 220–300 K for the (1–0) band (125–145 km altitude).

Keywords: carbon monoxide – non-LTE processes – planetary atmosphere – Venus

1 Introduction

A variety of non-LTE emissions have been observed on Venus. The dayside airglow includes emission of CO in the Fourth Positive bands, along with numerous atomic and ionic emissions (Durrance et al. 1980). In particular, the atomic O 130 nm airglow sounds the dynamical activity (e.g. waves) of Venus' upper atmosphere in a layer centred near 155 km (Alexander et al. 1993). On the nightside, the ultraviolet (198 nm) NO(0–1) nightglow, produced by the recombination of N and O atoms, is a sensitive tracer of the circulation

*Based on observations carried out at the Canada-France-Hawaii Telescope (CFHT), operated by the National Research Council of Canada, the Centre national de la recherche scientifique of France, and the University of Hawaii.

†Corresponding author, Tel.: 33145077599, Fax: 33145077939, email: jacques.crovisier@obspm.fr

at 115–150 km (Stewart et al. 1980, Gérard et al. 1981, Bougher et al. 1990). A similar constraint is provided by the O_2 Herzberg II nightglow at 400–800 nm, observed from Venera 9 and 10 (see Krasnopolsky 1983) and Pioneer Venus (Bougher and Borucki 1994) which probes the altitude range 100–130 km. O_2 emits also a similar, but much stronger (several megarayleighs (MR)), infrared airglow at 1.27 μm, which probes the 95–110 km region and exhibits spectacular spatial and temporal variations, although the dynamical and/or chemical processes controlling its detailed structure remain poorly understood (see reviews in Crisp et al. 1996, Lellouch et al. 1997). More recently, nightglow emission from the oxygen green line at 558 nm has been discovered (Slanger et al. 2001). At longer (mid-IR) wavelengths, non-LTE emission from CO_2 has been observed at 4.3 μm (Shirley et al. 1995) and 10 μm (Deming et al. 1983) on Venus' dayside.

In this paper, we report on observations of another airglow on Venus' dayside, due to emissions in the CO v(1–0) and v(2–1) vibrational bands at 4.7 μm, and probing the thermosphere at 100-150 km. Our original discovery of these emissions on Venus, using the Fourier Transform Spectrometer (FTS) at the Canada–France–Hawaii Telescope (CFHT), dates back to 1987 (de Bergh et al. 1988) but these observations have not been published in detail so far. These CO emissions have also been detected from NIMS/Galileo observations in horizontal viewing (Shirley et al. 1995) but incompletely published. Billebaud et al. (1991) presented the detection of similar emissions at Mars in 1989, and gave a succinct description of the mechanisms involved. Such emissions from CO have also now been seen on Titan (Lellouch et al. 2003, López-Valverde et al. 2005) and Uranus (Encrenaz et al. 2004). In this paper, we present in Section 2 the Venus observations, which include the spectra obtained in 1987 as well as improved Venus data recorded in 1994, using the same instrumental configuration (FTS at the CFHT) for several regions on the planet. From the higher quality 1994 observations, we derive in Section 3 individual line intensities and rotational distributions. A detailed modelling of the non-LTE processes leading to CO emissions is presented in Section 4. Although this model is applied to Venus in the present paper, it also pertains to Mars, as was briefly presented in Billebaud et al. (1991). A comparison between observations and models is made in Section 5, where the line intensities and the temperatures probed in two layers centred at 100–110 km and 125–145 km are discussed.

2 Venus observations

2.1 The first detection of CO infrared emission

On 10 January 1987 (UT), we observed Venus as a morning object with the high-resolution FTS at the 3.6-m CFH telescope in an attempt to look for unidentified minor constituents in its troposphere. The Venus phase angle was 90°. The spectra cover the 2000–2200 cm^{-1} range at an unapodized resolution of 0.039 cm^{-1}. The Doppler shift due to Venus' motion was 0.1 cm^{-1}. We used a 5″ circular aperture, centred on the brightest part of Venus' dayside, i.e. on the equator and about half-way between the terminator and the limb. Two spectra were obtained on this point, with a total of 38 min integration. For comparison, a Moon spectrum was recorded with the same filter and resolution.

[Figure 1 here]

Our search for unidentified minor species was unsuccessful but, most interestingly, we detected carbon monoxide emissions which had not been seen before, nor had they been predicted (de Bergh et al. 1988). Fig. 1 shows an expanded view of the spectrum at 2130–2160 cm^{-1}. A number of emission lines belonging to the P and R branches of the $v(1–0)$ fundamental of CO appear in the bottom of the strong and broad Venus CO absorptions, which are themselves blended with the telluric CO absorptions. In addition, emission lines of the $v(2–1)$ band of CO are observed. Since this band is intrinsically very weak in thermal emission (about 10^7 times weaker than the (1–0) band at 250 K), there are no corresponding absorptions detectable in the Venus spectrum. The presence of strong emission from the (2–1) band indicates a non-thermal mechanism. de Bergh et al. (1988) suggested that CO fluorescence excited by solar infrared radiation and CO prompt emission following CO_2 photolysis could account for this emission.

All the observed emission lines are clearly narrower than the instrumental resolution. Presumably, their intrinsic width is determined by Doppler broadening (half width at half maximum is 0.0025 cm^{-1} at 200 K). The strongest lines show up with a contrast of about 70 % of the continuum at the instrumental resolution.

2.2 Mapping of the CO emissions in 1994

Venus observations were obtained again on 22 and 23 September 1994 (UT) with the FTS at the CFHT, at an improved spectral resolution of 0.012 cm^{-1} (unapodized), giving a mean resolving power of 180 000 over the 2070–2180 cm^{-1} range of the CO 4.7 μm filter. The main goals were: (i) to make high S/N measurements of individual line intensities, (ii) to accurately determine the rotational temperature, and (iii) to measure absolute wind velocities at several places on the disk of Venus from Doppler shift. Venus had, at that time, an apparent diameter of 36″ and appeared in the sky as a bright evening crescent (phase = 0.30–0.31). Given the interpretation of the initial measurements (de Bergh et al. 1988), the emphasis of the observations was put on Venus' dayside. A 5″ circular aperture was again used and successively positioned on four different points on the illuminated crescent. These points are labelled 1, 3, 5, 6 (Fig. 2 and Table 1). In the original planning of the observations, an additional point (labelled 2) was located between points 1 and 3; however, it was finally not observed. Points 1 and 4 sample Venus' equatorial regions at central local times (LT) of 3:40 pm and 5:20 pm, while points 3 and 6 probe higher latitudes (42° S and 54° N respectively) near 5 pm LT. A spectrum was also obtained on Venus' nightside near disk centre (point 5) to check that the emissions were not present there. Tracking and position control of points on the Venus disk were performed by means of a visible image of Venus displayed on a TV screen. Spectra correspond to averages of 2 to 6 individual scans obtained from interferograms recorded in about 18 min. The need for relatively short integration times per scan (in spite of the very high spectral resolution desired) was dictated by the fine frequency corrections that are required for the wind measurements. A few individual scans were lost due to technical (electrical) problems, leaving total integration times of 35 to 105 min, depending on the target point (Table 1). Observations on 22 September were interrupted by a telescope failure shortly

Table 1: 1994 observations: Positions* of the 5 target points and continuum flux levels.

Point	latitude	Venus LT	date (Sept. 1994) / integration time	continuum flux**	
				relative	absolute
1	6° N	3:40 pm	22 / 70 min, 23 / 18 min	4.8	0.300
3	42° S	5:10 pm	22 / 70 min, 23 / 35 min	4.4	0.275
4	6° N	5:20 pm	22 / 18 min, 23 / 70 min	5.0	0.31
5	6° N	7:35 pm	23 / 35 min	3.2	0.20
6	54° N	4:50 pm	23 / 35 min	4.0	0.25
Mars	disk average		23 / 105 min		

* Position of the aperture centre

** At 2140 cm^{-1}; absolute flux units are erg s^{-1} sr^{-1} cm^{-2}/cm^{-1}

before Venus set, so that no comparison spectrum could be taken on another source. On 23 September, a spectrum of the Moon was recorded, at approximately the same airmass as Venus' observations, in order to correct for the telluric absorptions (primarily due to atmospheric CO, H_2O and N_2O). In total, seven independent spectra were recorded on Venus dayside (see Table 1), which will be analyzed independently. In addition, a spectrum of Mars (whose apparent diameter was 5.7″) was taken on 23 September with the same filter, resolution and 5″ aperture. CO 4.7-μm emissions have been observed previously on Mars (Billebaud et al. 1991), and the Mars spectrum was used as a check of the absolute frequency scale in an attempt to measure wind velocities for Venus. However, our results on the measurements of the wind velocities (a preliminary version of which had been given in Maillard et al. 1995) finally turned out to be inconclusive and will not be discussed any more in this paper. For all spectra (Venus, Mars, Moon), the noise level was determined by examining the signal fluctuations outside the filter. Typical signal-to-noise ratio in the continuum is of order 30 for each of the Venus points, 40 for the total Mars spectrum and 150 for the Moon spectrum.

[Figures 2 and 3 here]

The overall structure of the CO emissions is illustrated in Fig. 3a, for the example of point 1. (To avoid the presence of spurious additional emission lines due to imperfect correction of the telluric absorptions in the Venus/Moon ratio, the spectra in Fig. 3 are shown before division by the Moon spectrum). 25 lines belonging to the 1–0 band (from P 17 to R 10) and 24 to the 2–1 band (from P 9 to R 15) are detected. The large number of detected lines makes possible a determination of the rotational distribution (Section 5). The lines are still not resolved at the 0.012 cm^{-1} resolution, as expected, and the strongest lines show up with a contrast of $\sim$ 200 % of Venus' continuum. Typical signal-to-noise ratios on the line intensities are 20–50. In contrast, no emission is present on the nightside (point 5, Fig. 3b), consistent with the proposed emission mechanisms (de Bergh

et al. 1988; and Section 4), and implying a radiative de-excitation time much shorter that horizontal transport. In fact, transport over a 1 hr LT interval across the terminator (= 1580 km at Equator) by a typical total horizontal flow of 200 m/s takes about 2 hours, much longer than the radiative time for the $v = 1$ and 2 levels (a fraction of a second, as detailed below in Section 4). Therefore, the CO emissions must disappear very abruptly across the terminator (unlike e.g. the $O_2(^1\Delta)$ emissions at 1.27 μm; Crisp et al. 1996). Fig. 3c shows the Mars spectrum, which presents the same emission lines, although with a lower emission/continuum contrast. As is clear from the comparison of Fig. 1 and the right part of Fig. 3, the data from 1994 are of much higher quality than the original 1987 data. In particular, the higher spectral resolution (by a factor of 2.5) causes the spectrally unresolved (1–0) emissions to rise well above the continuum in these data, unlike in 1987. In addition, higher J lines are detected, e.g. up to (2–1) R 15 in 1994 vs. R 10 only for the 1987 data. The 1987 observations have therefore mostly an historical interest, and in what follows, we focus on the 1994 data.

3 Emission rates from the 1994 observations

3.1 Calibration of the continuum and relative contributions of the thermal and reflected components

Since we did not record any stellar spectrum, we did not obtain a direct flux calibration of the Venus spectra. However, the relative continuum flux levels at the 5 target points are determined in the measurements (Table 1), and the emissions can be calibrated in continuum units. Venus' spectrum at 4.7 μm is the sum of a thermal component, due to the cloud top emission, and of a solar reflected component, corresponding to the reflection of a fraction of the sunlight by the clouds. The thermal component is well known from extensive measurements on the nightside, especially from NIMS/Galileo (Carlson et al. 1991, Roos et al. 1993, Roos-Serote et al. 1995). The continuum flux at point 5 (nightside) can therefore be calibrated using the NIMS spectra, and the continuum flux at other points may then be determined by comparison to point 5. We use for calibration the radiance at 2140 cm^{-1}, a region essentially devoid of CO_2 absorption lines. From the NIMS spectra at low latitudes and low emission angles (Roos et al. 1993), we estimate a continuum radiance of 0.20 erg s^{-1} sr^{-1} cm^{-2}/cm^{-1} at this wavenumber for point 5 (i.e. a brightness temperature $T_B = 232$ K). This leads to the absolute radiances given in Table 1 for the five target points. The radiances determined in this manner for each spectrum are probably accurate to within 10 %. However, their interpretation in terms of continuum radiances at Venus is subject to pointing uncertainties, in particular for points 1, 3, and 6, which lie very close to the limb. For example, a 1.5″ pointing offset could lead, in the worst case, to a 28 % loss of flux for these limb points. Given the seeing fluctuations, such a pointing error cannot be excluded.

A quantitative examination of the relative fluxes in Table 1 allows one to get a crude estimate of the relative contribution of the thermal and reflected components to the total flux. The thermal component would be uniform over the disk if the temperature of the cloud region probed by this emission were constant both vertically and horizontally. However, the finite scale height of the clouds (about 5 km) and the negative temperature

lapse rate in the cloud top region ($dT/dz \sim -3$ K/km) induce a limb darkening of the thermal component. Such a limb darkening has been studied from ground-based (Diner 1978) and Pioneer Venus (Taylor et al. 1980) observations at 8–20 μm and more recently from NIMS/Galileo observations at 3–5 μm (Roos et al. 1993) outside the CO_2 bands. For example, Roos et al. (1993) determined a fit of the limb darkening profile at 4.00 μm and 0° latitude, as $T(\mu) = 233.5 - 11.9 \ln(\mu)$, where $T(\mu)$ is the brightness temperature (in K) at airmass μ (= 1/cos(emission angle)). We have retained this emission angle dependence to estimate the variation of the thermal flux between the three low latitudes points (1, 4 and 5). This equation, however, cannot be used for the high latitude points 3 and 6, because limb darkening curves are very sensitive to latitude above 40° (due to the variations with latitude of the vertical temperature gradient). We instead estimated the thermal flux at these points directly from NIMS measurements at similar emission angles and latitudes. Estimated thermal fluxes at 2140 cm^{-1} are thus 0.125, 0.14, 0.18, 0.20 and 0.13 erg s^{-1} sr^{-1} cm^{-2}/cm^{-1} for points 1, 3, 4, 5 and 6 respectively. The variation of the reflected component with observing geometry was computed by assuming the clouds act as a Lambertian reflecting surface. Although our field of view is not small compared to the size of the illuminated crescent, in all our calculations of the emission and incidence angles, we have simply used the position of the aperture centre rather than integrating over the aperture. With these simple assumptions, an estimate of the overhead reflected solar flux and cloud albedo A can be obtained from each target point on the crescent (with our observing parameters, the reflected solar flux at 2140 cm^{-1} at zero incidence angle is equal to $6.7 \times A$ erg s^{-1} sr^{-1} cm^{-2}/cm^{-1}). Inferred albedos are 0.045, 0.11, 0.12, and 0.09 respectively for points 1, 3, 4 and 6, suggesting a cloud albedo of 0.09 ± 0.03 at 2140 cm^{-1}. The ratio of reflected to thermal component at zero incidence and emission angles is approximately 3. The variability in the inferred cloud albedo from point to point is likely due to (i) the uncertainty on the flux levels (e.g. increasing the measured flux level at point 1 by 28 % would lead to an albedo of 7.5 % instead of 4.5 %) (ii) our simplified treatment of the geometry and (iii) possibly the fact that the clouds are not Lambertian. We also note that our estimate of the albedo is consistent with the scattering and absorbing properties of the Venus' upper cloud. At 4.7 μm, mode 1 (resp. mode 2) cloud particles (for 75 % H_2SO_4) have a single scattering albedo $\omega_0 = 0.22$ (resp. 0.46) and an asymmetry parameter of 0.30 (resp. 0.55). Using Eq. (13) from Moroz (1983), we infer an albedo of 0.045 for mode 1 and 0.08 for mode 2.

3.2 Line intensities measurements

With the continuum levels absolutely determined in this manner, it is possible to calibrate the line emissions. A preliminary order of magnitude can be obtained as follows. The strongest lines have an equivalent width of $0.012 \times$ 200 % = 0.024 cm^{-1}, in continuum units. For point 1, this corresponds to an intensity of $0.3 \times 0.024 = 7.2 \times 10^{-3}$ erg s^{-1} sr^{-1} cm^{-2}. Taking an average photon wavenumber of 2140 cm^{-1}, this intensity corresponds to 1.7×10^{10} photon cm^{-2} s^{-1} sr^{-1}, or 0.21 MR.

Many of the lines fall in regions of low atmospheric transmission (particularly the lines of the (1–0) band, which fall close to their CO absorption counterparts in the Earth spectrum). This frequency-variable atmospheric transmission must be taken into account to properly estimate emission rates and associated error bars. We proceeded as follows,

for each Venus spectrum. The Venus spectrum was first divided by the Moon spectrum in those spectral regions where the flux in the Moon spectrum was at least 5 % of the local continuum. Each frequency point of the ratioed (Venus/Moon) spectrum was assigned a signal-to-noise level, according to $1/\mathrm{SN}^2_{\mathrm{ratio}} = 1/\mathrm{SN}^2_{\mathrm{Venus}} + 1/\mathrm{SN}^2_{\mathrm{Moon}}$, where $\mathrm{SN}_{\mathrm{spectrum}}$ is the frequency-dependent signal-to-noise ratio in a given spectrum. Next, the ratioed spectrum was split in small frequency intervals centred around the individual CO emission lines and the line profiles were fit by the sum of a Gaussian and a straight line minimizing χ^2. Once the "pseudo-continuum" was known, the line area was determined either from the parameters of the Gaussian fit or from direct numerical integration of the spectrum with the pseudo-continuum removed. The two methods gave similar results within 5–10 %. Because the emission lines are not spectrally resolved, the relative uncertainty on their area was taken to be equal to the relative uncertainty on the line contrast in the ratioed spectra. The measured intensities for individual lines are reported in Section 5 and Figs 9 and 10 where a comparison with models is made. The calibration of the line intensities based on the continuum levels does not introduce any additional calibration uncertainty, but leads to frequency-variable error bars, depending on the position of the individual lines with respect to the telluric absorptions.

4 Modelling CO non-LTE emission

As briefly mentioned previously, given the relatively low kinetic temperatures in the Venus (or Mars) atmospheres at the levels where the lines are likely to be formed (200 K or less), the observed CO emission lines cannot originate from molecules at LTE: at 200 K, the $v \geq 1$ levels are practically not populated (their total population being less than 2×10^{-7} that of $v = 0$). Therefore, mechanisms which could drive CO out of equilibrium need to be invoked to explain the emissions. The CO emitting region must be in the upper atmosphere, where collisions are rare and cannot quench excitation mechanisms.

In the next subsection we will review some relevant physical processes involving CO in the upper atmosphere of Venus (and Mars, see Billebaud et al. 1991), and make order-of-magnitude evaluations of CO emission. In the following subsection, we will present a more elaborate quantitative model which will be compared to observations in Section 5.

4.1 An overview of physical processes

Two competing mechanisms may excite molecules in the low-density regions of the upper atmosphere: radiative excitation followed by fluorescence, and chemical reactions creating the molecules in excited energy states. Radiative excitation drives the 10–μm line emissions of CO_2 observed in the spectra of Venus and Mars (Betz et al. 1976; Johnson et al. 1976; Deming et al. 1983; Deming and Mumma 1983). Emission at visible or UV wavelengths following photolysis is a well known aeronomic process responsible for the airglow, which is likely to occur also at infrared wavelengths. $v(1\text{–}0)$ ro-vibrational lines of CO were detected in the atmosphere of comet C/1996 B2 (Hyakutake) (Mumma et al. 1996) and were since observed in many other comets. Fluorescence is a likely mechanism for their emission as was predicted by earlier studies (Crovisier and Le Bourlot 1983; Chin and Weaver 1984; Crovisier 1987).

Although not frequent enough to impose LTE, collisions are still important and their influence must be evaluated. For the CO column densities encountered here, the ro-vibrational lines are optically thick and radiative transfer effects have to be taken into account. For the atmosphere of Venus, we adopt the model (total density, CO and CO_2 densities, temperature) given in VIRA (Keating et al. 1985) at the subsolar point for altitudes between 100 and 250 km and the model of Seiff (1983) between 60 and 100 km. The temperature, CO and CO_2 density distributions are shown in Fig. 4.

[Figure 4 here]

4.1.1 CO fluorescence

For this process carbon monoxide is radiatively excited by the external radiative field (solar) and the local radiative field (scattered solar field and the planet thermal emission). In the UV, resonant fluorescence of the CO fourth-positive system $A^1\Pi$–$X^1\Sigma^+$ around 154 nm is a well-known component of Venus dayglow (Durrance et al. 1980; Durrance 1981). Its typical excitation rate (the so-called g-factor, which is the number of photons absorbed by second by molecule) is $g_{A-X} = 2.3 \times 10^{-6}$ s^{-1} for the whole system. For the $B^1\Sigma^+$–$X^1\Sigma^+$ system at 115 nm, $g_{B-X} = 10^{-6}$ s^{-1} (deduced from Krishna Swamy 1979). All excitation rates are given here for the quiet Sun and for an heliocentric distance of 0.73 UA, corresponding to the mean Venus–Sun distance.

Radiative cascades will lead to various vibrational states of the electronic ground state. The $v = 1$ and 2 states will thus be excited with rates of the order of 2×10^{-6} s^{-1} (Fig. 5).

[Figure 5 here]

The vibrational levels of CO will also be directly excited by the infrared radiation field. Following Crovisier and Encrenaz (1983), the rate due to a blackbody of temperature T_{bb} seen over a solid angle Ω_{bb} is:

$$g_{ul} = \frac{\Omega_{bb}}{4\pi} \frac{\omega_u}{\omega_l} A_{ul} \left[\exp\left(\frac{hc\sigma_{ul}}{kT_{bb}}\right) - 1 \right]^{-1} \quad (1)$$

where ω_l and ω_u are statistical weights of the lower (l) and upper (u) levels, A_{ul} is the Einstein coefficient for spontaneous emission and σ_{ul} is the wavenumber of the transition. For the unattenuated solar radiation field ($T_{bb} = 5770$ K and $\Omega_{bb} = 1.28 \times 10^{-4}$ sr), this leads to (Fig. 5):

$g_{1\leftarrow 0} = 4.6 \times 10^{-4}$ s^{-1} for infrared excitation of the CO $v = 1$ level;
$g_{2\leftarrow 0} = 5.0 \times 10^{-6}$ s^{-1} for infrared excitation of the CO $v = 2$ level;

and much smaller rates for higher vibrational levels. Only excitation from $v = 0$ is considered here. Einstein coefficients have been computed from Goorvitch and Chackerian (1994). The subsequent emission rates for infrared fluorescence are:

$g_{2\to0} = 7.5 \times 10^{-8}$ s^{-1},
$g_{2\to1} = 4.9 \times 10^{-6}$ s^{-1},
$g_{1\to0} = 4.6 \times 10^{-4}$ s^{-1}.

Therefore, infrared excitation by the Sun is dominant with respect to UV excitation. Thermal emission from Venus is a minor source of excitation (≈ 3 % for the $v = 1$ level and negligible for the $v = 2$ level). In optically thin conditions, the $v = (1–0)$ band should be two orders of magnitude more intense than the $v = (2–1)$ band. We will see later that radiative transfer could drastically change this order of things.

4.1.2 CO excitation due to CO_2 photolysis

In the upper atmosphere of Venus, the main process leading to the creation of carbon monoxide is the photodestruction of CO_2:

[1] $CO_2 + h\nu \longrightarrow CO\ (X^1\Sigma^+) + O\ (^1D)$ rate $= 1.80 \times 10^{-6}$ s^{-1},
[2] $CO_2 + h\nu \longrightarrow CO\ (a^3\Pi) + O$ rate $= 0.54 \times 10^{-6}$ s^{-1}.

The rates are derived from Huebner et al. (1992), for unattenuated solar UV at the heliocentric distance of Venus. The energy of the photodissociating photons is generally much larger than the binding energy of CO_2: the excess energy is converted to electronic, vibrational, rotational or translational energy to the fragments. To know the relative distribution of these different forms of energy, detailed laboratory investigations of CO_2 photolysis for the whole wavelength region of the solar spectrum would be needed. Only partial data are available.

For channel [1], indirect measurements were made by Welge and Gilpin (1971) through measurement of the energy of the oxygen atom by time-of-flight spectroscopy. Although no quantitative evaluation is given, it was concluded that in the wavelength range 105–116 nm, more than 50 % of the dissociation leads to CO in the electronic ground state ($X^1\Sigma^+$), but with considerable amounts of vibration-rotation energy.

For channel [2], the fluorescence of the CO ($a^3\Pi$–$X^1\Sigma^+$) Cameron bands was measured in the laboratory (Lawrence 1972). Approximate vibrational distributions have been determined: they are fairly flat over the first vibrational levels of CO.

In the absence of more comprehensive laboratory measurements, we assume that carbon dioxide photodestruction leads to vibrationally excited CO with an approximately flat distribution over the first $v \leq 9$ levels. Since vibrational de-excitation occurs preferentially by $\Delta v = 1$ steps, we can infer that for each creation of a CO molecule, about one photon will be emitted in each of the first ($v \to v - 1$) bands. Thus, in optically thin conditions, this mechanism would yield (1–0) and (2–1) emissions with approximately similar intensities.

Carbon dioxide is photodissociated by solar photons in the range $0 < \lambda < 170$ nm, where the total solar flux is 2.5×10^{12} photons s^{-1} cm^{-2} (from the quiet solar spectrum model of Huebner et al. 1992) at Venus. With the assumptions made above, this will result in total emissions of about 2 MR for the (2–1) band and 2.2 MR for the (1–0) band. At a rotational temperature of 200–250 K, this corresponds to about 2×10^5 R for the strongest ro-vibrational lines of these bands.

4.1.3 Collisional quenching

Vibrational quenching of CO by collisions with CO_2 has been studied experimentally by Starr and Hancock (1975). The main process is a transfer of vibrational energy from CO to CO_2:

$$\mathrm{CO}\ (v) + \mathrm{CO_2}\ (000) \longrightarrow \mathrm{CO}(v-1) + \mathrm{CO_2}\ (001) - 206\ \mathrm{cm^{-1}}.$$

The de-excitation rate of the $v = 1$ level is $\simeq 2 \times 10^3\ \mathrm{s^{-1}\ torr^{-1}}$ at 250 K, corresponding to a reaction rate $k\sigma < v >= 5.6 \times 10^{-14}\ \mathrm{cm^{-3}\ s^{-1}}$ (Starr and Hancock 1975), $< v >$ being the average collision velocity. Below $z = 105$ km, where the density is larger than $5 \times 10^{14}\ \mathrm{cm^{-3}}$, collisional de-excitation is larger than vibrational decay rate ($A \simeq 30\ \mathrm{s^{-1}}$), and quenching is important. We assume that collisional de-excitation of the $v = 2$ level, for which no laboratory measurement has been found, is similar.

Following the reverse process, collisions with CO_2 (001) could in principle lead to vibrational excitation of CO. The CO_2 (001) relative population may be found from the model of Roldán et al. (2000). This process is negligible, however (M. López-Valverde, *personnal communication*).

The collisional cross-section for rotational transitions is only an order of magnitude smaller than the hard-sphere cross-section, typically $\simeq 10^{-16}\ \mathrm{cm^2}$. Thus, rotational relaxation is much faster than radiative rotational decay of CO, which has very small rotational A_{ij}'s (for instance $A_{J6\to5} = 2 \times 10^{-5}\ \mathrm{s^{-1}}$ whereas the collision rate $n\sigma < v > \simeq 10^3\ \mathrm{s^{-1}}$ below $z = 105$ km). Therefore we can confidently assume that the rotational distribution of CO is thermal within each vibrational state.

4.1.4 Radiative transfer

At temperatures encountered in the atmospheres of Venus and Mars, the CO molecules would be concentrated in the $v = 0$ vibrational level. Therefore, the (1–0) lines will be optically thick for the column densities of CO in the atmosphere. The (2–0) lines will be thinner (because $A_{2\to0}$ is much smaller than $A_{1\to0}$). The (2–1) lines are thin because the $v = 1$ level is not significantly populated. Since the upper level is much less populated than the lower level, the optical depth of a line $u \to l$ is:

$$\tau_{ul} = \frac{1}{8\pi\sigma_{ul}^3}\frac{1}{\Delta v}A_{ul}N_l \qquad (2)$$

where N_l is the column density of the lower ro-vibrational state, and Δv is the line width (in velocity units). For CO at 200 K, $\tau \simeq 1$ is reached for the strongest ro-vibrational transitions of the (1–0) band for a total CO column density $N_{\mathrm{CO}} = 5 \times 10^{15}\ \mathrm{cm^{-2}}$, which corresponds to $z = 150$ km. For the (2–0) band, these figures are respectively $N_{\mathrm{CO}} = 1.2 \times 10^{17}\ \mathrm{cm^{-2}}$ and $z = 105$ km.

Thus, one effect of radiative transfer will be to enhance the (2–1)/(1–0) emission intensity ratio. Since the (1–0) lines are optically thick at an altitude much higher than the altitude where collisional de-excitation occurs, their emission will be limited by optical depth effects rather than by collisional quenching.

The total solar energy flux absorbed in a thick line is $F(\sigma)\Delta\sigma$, where $F(\sigma)$ is the solar flux density (taken here as that of a 5770 K blackbody), and $\Delta\sigma$ is the line width (about

0.6 km s^{-1} for CO at 250 K). This corresponds at Venus to 2.3×10^{11} and 6.2×10^{11} photons cm^{-2} s^{-1} for the lines of the (1–0) and (2–0) bands of CO, respectively. After fluorescence and possibly multiple scattering for the (1–0) band, we obtain intensity estimates of 6×10^5 and 8×10^5 rayleighs for the ro-vibrational lines of the (2–1) and (1–0) bands, respectively. These intensities are comparable to the observed emission rates.

4.2 A quantitative model

We have shown in the previous section that fluorescence and prompt emission of CO following CO_2 photodissociation are mechanisms which can yield the emission of CO vibrational lines with intensities comparable to those observed in Venus and Mars. This justifies a more sophisticated quantitative treatment of these processes, which will now be presented.

Our model evaluates the emergent CO infrared emission fluxes, taking into account solar infrared radiation, ultraviolet excitation through the fourth-positive system of CO, vibrational excitation of CO following CO_2 photolysis, radiative transfer, and collisions. We have included the CO ro-vibrational levels up to $v = 3$ and $J = 25$. Higher vibrational and rotational levels appear to have little influence on the excitation. As the 5-μm continuum in Venus' spectrum is formed at the optically thick cloud top level (60 km), the atmosphere below the clouds does not contribute to the emerging 5-μm radiation. This altitude is set as a limit for radiative transfer integration.

The atmosphere is assumed to be plane-parallel, illuminated by the Sun with a zenithal angle Φ_s and observed at a zenithal angle Φ_o. The principle of the computation is to integrate optical depths and line intensities from an altitude $z = \infty$ to $z = 60$ km. The CO relative populations P_i (i = ro-vibrational levels by increasing energy) are computed at each altitude z by solving the micro balance equations:

$$\frac{dP_i(z)}{dt} = \left[\begin{array}{c}\text{collision}\\ \text{terms}\end{array}\right] + \left[\begin{array}{c}\text{radiative}\\ \text{excitation}\\ \text{terms}\end{array}\right] + \left[\begin{array}{c}\text{spontaneous}\\ \text{emission}\\ \text{terms}\end{array}\right] + \left[\begin{array}{c}\text{chemical}\\ \text{terms}\end{array}\right] = 0 \qquad (3)$$

$$\Sigma P_i(z) = 1. \qquad (4)$$

A major simplification in our model is the assumption of *local approximation*, described in Section 4.2.3, which allows us to solve for $P_i(z)$ with a single integration over z, without any iteration between radiation field and CO relative populations. Other simplifications are the adoption of a uniform kinetic temperature for the atmosphere, and of rectangular shapes for the ro-vibrational lines.

4.2.1 The collision terms

We distinguish between collisions inducing rotational transitions, and collisions inducing vibrational transitions. We assume that each (rotational or vibrational) collision redistributes the molecule according to the (rotational or vibrational) Boltzmann distribution. Then collisions are fully described by the kinetic temperature T_k and the total collision rates C_r and C_v inducing respectively rotational and vibrational transitions. Thus,

$$C_r = n\sigma_r < v >, \tag{5}$$

$$C_v = n\sigma_v < v >, \tag{6}$$

with the average collision velocity being

$$< v >= \Big[\frac{8kT_k}{\pi}[\frac{1}{m_{\rm CO}} + \frac{1}{m_{\rm CO_2}}]\Big]^{\frac{1}{2}}. \tag{7}$$

We have assumed that CO_2 is the only collision partner to CO. The collisional term in the steady state balance equation is

$$\Big[\frac{dP_i(z)}{dt}\Big]_{\rm coll.} - P_i(z)C_r(z) + P_i^t(T)C_r(z)\sum_j P_j(z) - P_i(z)C_v(z) + P_i^t(T)P_{vib}^t(T)C_v(z), \tag{8}$$

where $P_i^t(T)$ and $P_{vib}^t(T)$ are the rotational and vibrational Boltzmann distributions at the local temperature. We assume $\sigma_v < v >= 5.6 \times 10^{-14}$ cm^3 s^{-1} at 250 K (Starr and Hancock 1975) and $\sigma_r = 10^{-16}$ cm^2. The practical effect of C_r is to ensure rotational LTE in each vibrational level (and thus the exact value of σ_r is not critical), and that of C_v is to quench the vibrational levels at low altitudes.

4.2.2 The radiative excitation terms

Excitation by attenuated solar radiation may be written as:

$$\Big[\frac{dP_i(z)}{dt}\Big]_{\rm rad.} = -P_i(z)\sum_{j>i} g_{ij}(z) + \sum_{j<i} P_j(z)g_{ji}(z), \tag{9}$$

where the excitation rates (see Crovisier and Encrenaz 1983) are defined as:

$$g_{ij}(z) = \frac{1}{8\pi h\sigma_{ji}^3}\frac{2J_j+1}{2J_i+1}A_{ij}\mathcal{J}(\sigma_{ji})\exp(-\frac{\tau_{ij}(z)}{\cos\Phi_s}), \tag{10}$$

J_j and J_i being the rotational quantum numbers, $\mathcal{J}(\sigma_{ji})$ the unattenuated solar radiation, and $\tau_{ij}(z)$ the zenithal line optical depth from z to ∞. The solar spectrum is assumed here to be that of a blackbody at 5770 K. We estimate that using a more accurate continuum solar spectrum, such as that of Labs and Neckel (1968), and taking into account the CO absorption lines in the solar spectrum (as observed by the ATMOS experiment; Farmer and Norton 1989) would not drastically affect our results. We have not taken into account here excitation due to multiple scattering of external radiation, or de-excitation by spontaneous emission. These effects will be included as radiation trapping effects in the next subsection.

In the present model, we consider radiative excitation from the $v = 0$ level only (which represents more than 0.9999 of the total CO population). The CO rotational population of this vibrational level is the same everywhere, since rotational LTE is ensured by collisions and we have assumed uniform T_k. Then, for rectangular line shapes, τ_{ij} is proportional to the total CO column density $N_{\rm CO}(z)$ between z and ∞; thus

$$\tau_{ij}(z) = \frac{1}{8\pi\sigma_{ij}^3}\frac{A_{ij}}{\Delta v}P_i^t(z)N_{\rm CO}(z), \tag{11}$$

where Δv is the line width in velocity units.

4.2.3 The spontaneous emission terms and radiation trapping

In the optically thin case, the spontaneous emission terms are:

$$\left[\frac{dP_i(z)}{dt}\right]_{\rm spont.} = -P_i(z)\sum_{j<i}A_{ij} + \sum_{j>i}P_j(z)A_{ji}. \tag{12}$$

Lines with lower levels in the $v = 0$ state may be extremely optically thick. For them we must take into account radiative trapping: absorption, as well as radiative excitation due to multiple scattering. An exact treatment would involve multiple-dimension integration and extensive iterations. In order to avoid prohibitive computer-time calculations, we used the *local approximation* and the *escape probability* formalism. The local radiation field due to multiple scattering is then assumed to be due to molecules having the local population distribution, and the micro balance equations may be resolved locally, avoiding iterations. The spontaneous emission terms thus become

$$\left[\frac{dP_i(z)}{dt}\right]_{\rm spont.} = -P_i(z)\sum_{j<i}A_{ij}\beta_{ij}(z) + \sum_{j>i}P_j(z)A_{ji}\beta_{ji}(z), \tag{13}$$

where β_{ij} is the escape probability

$$\beta_{ij}(z) = \frac{1}{4\pi}\int_{4\pi}\exp(-\tau)d\Omega. \tag{14}$$

τ is taken to be ∞ in the hemisphere toward the planet (no photon can escape in this direction), and $\tau = \tau_{ij}(z)/\cos\Phi$ outwards. Φ is zenithal angle and $\tau_{ij}(z)$ is defined by Eq. (11). After integration, we obtain

$$\beta_{ij}(z) = \frac{1}{2}[\exp(-\tau_{ij}) - \tau_{ij}{\rm Ei}(\tau_{ij})], \tag{15}$$

where Ei is the exponential integral function (${\rm Ei}(x) = -{\rm E}_1(-x)$).

4.2.4 The chemical terms

These terms are creation and destruction rates of CO at the altitude z. We assume steady state, so their sum is null and the total CO density is constant (the CO density does evolve with time, but its evolution is very slow compared to the collision and radiative rates considered here). CO is supposed here to come uniquely from the photodissociation of CO_2. Its creation rate is thus

$$S_{\rm CO}(z) = K(z)n_{\rm CO_2}(z), \tag{16}$$

where $K(z)$ is the CO_2 photodestruction rate at altitude z. Above the atmosphere, this rate is

$$K(\infty) = \int \sigma_{\mathrm{CO}_2}(\lambda) F(\lambda) d\lambda, \tag{17}$$

where $\sigma_{\mathrm{CO}_2}(\lambda)$is the CO_2 photoabsorption cross-section and $F(\lambda)$ is the solar ultraviolet radiation flux. Inside the atmosphere, attenuation of the solar flux must be taken into account, and the photodestruction rate becomes

$$K(z) = \int \sigma_{\mathrm{CO}_2}(\lambda) F(\lambda) \exp\left[- \frac{\sigma(\lambda) N_{\mathrm{CO}_2}(z)}{\cos \Phi_s} \right] d\lambda, \tag{18}$$

where $N_{\mathrm{CO}_2}(z)$ is the CO_2 zenithal column density between z and ∞. We have adopted the quiet solar spectrum model of Huebner et al. (1992) and the CO_2 photoabsorption cross-sections tabulated by Yung and Demore (1982) longward of 121 nm, those measured by Inn et al. (1953) between 105 and 121 nm. Shortward of 105 nm, photoabsorption by CO_2 leads to ionization rather than creation of CO, and has been neglected here. The resulting CO_2 photodestruction rate is 0.7×10^{-7} s^{-1} above the atmosphere of Venus. It drops by a factor of two at $z = 135$ km (for $\Phi_s = 30°$). New CO_2 cross-sections have been measured by Lewis and Carver (1983) with a better spectral resolution, showing a temperature dependence at long wavelengths. They have not been introduced in the present model.

We assume that CO is created in every vibrational state v with a flat distribution $P_v^{\mathrm{chem.}}$ over $1 \leq v \leq 9$ (see subsection 4.1.2), and in every rotational state with the Boltzmann distribution P_i^t at T_k. The chemical terms in the micro balance equations can then be written as

$$\left[\frac{dP_i(z)}{dt} \right]_{\mathrm{chem.}} = \frac{n_{\mathrm{CO}_2}(z)}{n_{\mathrm{CO}}(z)} K(z) [P_i^t(T_k) P_v^{\mathrm{chem.}} - P_i(z)]. \tag{19}$$

4.3 Results

The model has been run for a solar zenithal angle $\Phi_s = 60°$ and an observer zenithal angle $\Phi_o = 45°$, which typically corresponds to the geometry of the CFHT observation, and for various kinetic temperatures in the range 100–200 K. In Figs 6–8, we present the results for a temperature of 200 K only.

Fig. 6 shows the relative populations of the vibrational levels of CO as a function of altitude. The model has been applied with and without CO_2 photolysis, to evaluate the importance of this process. One can see from Fig. 6 that the $v = 3$ level is especially affected by this process. Indeed, fluorescence alone cannot significantly populate this level, due to the very small value of $g_{3 \leftarrow 0}$.

[Figures 6 and 7 here]

The volumic emissions $E_{ij}(z)$ of the CO molecules, as a function of altitude, are

$$E_{ij}(z) = hc\sigma_{ji} A_{ji} n_{\mathrm{CO}}(z) P_j(z) \exp\left(-\frac{\tau_{ij}(z)}{\cos \Phi_o}\right). \tag{20}$$

They are shown in Fig. 7 for the total emissions of the v(1–0) (2–1) and (3–2) bands. One can see that the z = 120–150 km layers contribute most to the (1–0) band, whereas the emissions of the (2–1) and (3–2) bands rather come from a lower altitude z = 90–120 km.

Finally, the emerging line intensities are computed as

$$I_{ij} = \int_{z_{lim}}^{\infty} E_{ij}(z) \frac{dz}{\cos \Phi_o}. \quad (21)$$

The corresponding synthetic spectra of the three bands are shown in Fig. 8.

[Figure 8 here]

There are obviously some shortcomings in this model, which limit its validity:

1. Branching ratios following CO_2 photodissociation are ill-known or even unknown: laboratory measurements would be welcome.

2. A *uniform* rotational temperature of CO is assumed all over the atmosphere, which is not realistic, but justified because the observed emissions are coming from a restricted altitude range. A check with a realistic temperature profile would be useful, however, but would imply a deep modification of the computing code.

3. *Local approximation* is assumed for radiative transfer. In a somewhat different context — the evaluation of the rotational level distribution of water in a cometary atmosphere — the results of a local approximation model were compared with those of a Monte Carlo code (Zakharov et al. 2005) based on the accelerated lambda iteration algorithm of Hogerheijde and van der Tak (2000). It was found that the results differed by only a few percent. Thus, we believe that this approximation does not introduce any strong bias in the results.

An improvement would be to use a line-by-line transfer code such as that applied by López-Valverde et al. (2005) to non-LTE CO emission in Titan. This is beyond the scope of the present paper.

5 Comparison of intensities with models and determination of rotational temperatures

We now compare the model with observational results. For each of the four dayside target points of the 1994 observations of Venus (points 1, 3, 4, 6), the measured intensities of the individual emission lines of CO (expressed in megarayleighs and determined according to the method outlined in Section 3) are shown in Figs 9 and 10 for the (2–1) and (1–0) bands, respectively, for the average of the 22 and 23 September data. These intensities have not been corrected for a potential backscattering effect by the underlying clouds. Although backscattering must occur, as is the case for the O_2 1.27 μm airglow, this effect is weak because the albedo at 4.7 μm is only ≈ 0.09.

[Figures 9 and 10 here]

The line intensities are in reasonable agreement with the models presented above, although they tend to be somewhat lower than predicted. As detailed below, the measured intensities are 0.3–0.8 time the predicted values for the (2–1) band and 0.4–1 time for the (1–0) band. Although the intensity measurements are more difficult for the (1–0) band than for the (2–1) band (because of the contamination by telluric and venusian CO $v(1\text{–}0)$ absorption lines adjacent to the (1–0) emission features), Figs 9 and 10 clearly show that the rotational distribution is very different for the two bands. The (2–1) band shows a familiar optically thin rotational distribution with a maximum of intensity for quantum numbers $J = 4$ or 5. In contrast, optical depth effects considerably flatten the distribution of the $v(1\text{–}0)$ band in such a way that no clear maximum can be distinguished. These features are in agreement with the models presented above. Model fitting of the observations allows one to determine rotational temperatures. Because the measured and predicted line intensities do not completely agree, an intensity multiplying factor is introduced in the model as a free parameter. The rotational temperatures and their error bars are determined by χ^2 minimization. In more details, for each model, a multiplicative factor k is determined by minimizing:

$$\chi^2 = \sum \left[\frac{Obs_i - k \times Model_i}{\sigma_i} \right]^2 \tag{22}$$

where Obs_i and σ_i are the individual line intensities measurements and their 1–σ error bars and $Model_i$ is the line intensity in the model. The retained rotational temperature is the one which provides the lowest overall χ^2. Results are given in Table 2 for the (1–0) and (2–1) bands and the various target points and observing days (seven measurements in total). The best model fits are superimposed on the data in Figs 9 and 10. The vastly different line distributions for the two bands can be overall accounted for by the models. However, the models do not fit all data points within the 1–σ error bars, probably suggesting an underestimate of the actual uncertainties. This is particularly true for the (1–0) band in general and for the lines of the P-branch of the two bands at 2080–2110 cm^{-1} (the reason being probably that this region is strongly affected by N_2O telluric absorption). Fig. 11 shows, on the example of point 1, the sensitivity of the models to changes in the rotational temperatures for the (1–0) and (2–1) bands.

[Figure 11 here]

For these best fits, the multiplicative factors for the (2–1) band are: 0.31, 0.40, 0.76 and 0.66 for points 1, 3, 4 and 6 respectively. For the (1–0) band, these factors are: 0.43, 0.65, 1.04 and 0.56, respectively. On average, the model overestimates the observed values by a factor of 2 for the (2–1) band and by a factor of 1.5 for the (1–0) band. It is noteworthy that model and observations agree quite well for point 4, and it may therefore be wondered if the discrepancy between model and observations could be due to a severe loss of flux for other points (for point 4, the observed continuum flux level is insensitive

to pointing errors). However, we note that a typical loss of flux by a factor of 3 for the limb points would imply a systematic pointing error of 3″, which we feel is not realistic. In addition, if the continuum fluxes are readjusted upwards so that the measured emission levels perfectly match the model predictions, then the cloud albedo at 5 μm (inferred as in Section 3) increases considerably. Specifically, cloud albedos inferred from points 1, 3, 4 and 6 become 0.17, 0.32, 0.14 and 0.32, or 0.24 on average, which is probably unrealistic given the optical properties of the H_2SO_4 clouds.

Therefore, although pointing errors may contribute, we are rather inclined to think that the factor of 1.5–2 difference reflects a model limitation rather than an error in the experimental calibration. We have adopted a simplified geometrical model, using a single value of the solar zenith angle ($\Phi_s = 60°$) and of the emission angle ($\Phi_o = 45°$) for all points. Actual values of Φ_s at aperture centres are 55° for point 1 and 80° for other points, while $\Phi_o = 34°$ for point 4 and 60° for other points. However, using these individual values would also not be completely satisfactory given the large aperture size, and a detailed modelling should calculate the excitation on a fine grid and average it over the apertures. This task, which is beyond the scope of this work, would probably lead to changes in the multiplicative factors k required to fit the data. However, we do not feel that our approximate geometrical modelling is the sole cause of the discrepancy, because the disagreement appears to be largest at point 4 ($k = 0.31$ and 0.43 for the (2–1) and (1–0) bands respectively), for which Φ_s and Φ_o are closest to our adopted values.

For all the models presented above, the VIRA dayside reference model (i.e. for the sub-solar point) was adopted. However, our 1994 observations rather sound the afternoon (local time = 3:40 to 5:20 for points 1, 3, 4, 6), while the CO_2 and CO number densities vary significantly with solar zenith angle. For example, at 150 km, the CO number density decreases by a factor of ~ 5 between SZA = 34 and 90°. Similarly, at 120 km, the difference in the CO mixing ratio between the VIRA dayside and nightside reference models is about a factor of 3. In addition, the CO mixing ratio in the upper mesosphere/lower thermosphere is known to significantly vary with time (Clancy et al. 1991, Lellouch et al. 1994). Therefore an error in the CO profile adopted in the model by a factor of several is quite possible, which would easily account for the disagreement with the observations, at least for the (2–1) band (the (1–0) band, being optically thick, should be less sensitive to the CO profile).

Another source of difference which might be thought of comes from the fact that the CO emissions in Venus' atmosphere are partly absorbed by the CO_2 column lying above the level from which they originate. This possible absorption is not considered in the models of Section 4. However, dayside CO_2 column densities above the 135 km (1–0) band and 105 km (2–1) levels are $\sim 6\times10^{16}$ cm^{-2} and 1×10^{20} cm^{-2}, respectively. Assuming a (Doppler) line width of 2×10^{-3} cm^{-1} for the CO_2 lines, the lines that could contribute a significant ($\tau \sim 1$) opacity must have intrinsic strengths (at ~ 200 K) of at least 6×10^{-20} cm/mol and 3×10^{-23} cm/mol for the (1–0) and (2–1) bands respectively (and of course coincide in frequency with the CO lines within $\sim$ 1 Doppler width). No CO_2 lines in this spectral range have line strengths larger than 10^{-22} cm/mol. About 15 individual lines are stronger than 10^{-23} cm/mol but they no dot coincide with any of the lines of the CO v(2–1) band. The only significant CO_2 absorption is probably due to a family of lines near 2093.4 cm^{-1} which affect the radiation emitted in the CO v(2–1) $P6$ line at

Table 2: Rotational temperature measurements (K).

Point	band (1–0)			band (2–1)		
	22 Sept.	23 Sept.	Average	22 Sept.	23 Sept.	Average
1	252±50	270±70	260±40	190±16	183±16	187±11
3	260±45	262±60	260±35	194±30	203±40	198±24
4	251±34	248±35	250±25	190±20	170±24	182±15
6		270±40			200±16	

2093.411 cm^{-1}. Therefore, we conclude that, with this exception, the absorption by CO_2 in Venus' atmosphere has a negligible impact on the CO v(1–0) and (2–1) emission bands. In summary, we think that the factor of 1.5–2 difference between observed and modelled intensities may be due to a combination of (i) flux losses at limb points, (ii) our simplified treatement of the observing geometry and (iii) a spatially and temporally variable CO profile.

6 Discussion and conclusions

We have obtained rotational temperatures at two levels. Temperatures for the v(2–1) band are in general agreement with the physical temperatures on Venus' dayside atmosphere at 100–110 km, as can be seen from a comparison with the Pioneer-based tabulation of diurnal and latitudinal temperatures by Taylor et al. (1985). At a nominal altitude of 107 km, and a latitude of 5° N, Taylor et al. (1985) give $T = 195$ K in the 2 pm–4 pm LT range and $T = 180$ K at 4 pm–6 pm. This compares favourably with our measurements at points 1 and 4 (187±11 K and 182±15 K, respectively). For points 3 and 6, we obtain $T = 198 \pm 24$ and 200±16 K, marginally higher than the Taylor et al. values at 45–55° N and 4 pm–6 pm (172–175 K). This confirms that the rotational populations are thermalized and validates the model of Section 4 in terms of the sounded altitude. However, the error bars on our derived temperatures appear to be too large to safely determine temperature differences from point to point (in particular variations with latitude). Temperatures inferred from the v(1–0) band — typically 260±40 K for all points — are somewhat higher than expected at 125–145 km. For example, the VIRA dayside reference model (Keating et al. 1985) has $T = 198$ K at 125 km, 215 K at 135 km and 236 K at 145 km. Similarly, at 135 km and 3 pm–5 pm (an LT range appropriate for comparison with our observations), Bougher et al. (1988b) predict T ∼ 180–215 K. Since the dayside temperature increases very rapidly with altitude in this atmospheric region, this might suggest that the altitude probed by the v(1–0) emissions is slightly higher than predicted in Section 4.

Temperature measurements in Venus' thermosphere were obtained in two separate layers, at 100–110 km and at 125–145 km. The mean rotational temperatures, weighted-averaged over the seven measurements, are 189 ± 8 K and 257 ± 16 K for the (2–1) and (1–0) bands, respectively. These clearly different values are another proof of the non-LTE character of the emissions and confirm that the rotational populations are in thermal equi-

librium at the relevant altitudes. On the other hand, measuring the temperatures from rotational distributions with an accuracy sufficient to obtain significant dynamical information (i.e., within $\sim$ 5 K) would require to improve the signal-to-noise ratio by a factor $\sim$ 3–5, compared to what is obtained here. An accurate determination of the continuum level would also be necessary, which may be difficult in a spectral region crowded with telluric lines.

In summary, we have finally reported on the 19–year old detection of CO emission lines at 4.7 μm from the Venus atmosphere. Models invoking CO fluorescence (as in Mars, Titan, and Uranus) and photodissociation of CO_2 into CO excited states (also contributing to the Mars case) were achieved. The CO radiative excitation by solar infrared radiation is the dominant process responsible for the emission of the v(1–0) and (2–1) bands. CO_2 photolysis adds a secondary contribution to the v(2–1) band emission and would be the main process for the (not yet observed) v(3–2) band emission. Both processes are switched off on the nightside, and the radiative lifetime of the CO excited levels is short, which explains the absence of the CO emissions on the dark side. These models appear to reproduce the order-of-magnitude of the observed emissions — although discrepancies by a factor of 1.5–2 remain — and to match the very different rotational structure of the v(1–0) and (2–1) bands. Temperature determinations are in reasonable agreement with previously inferred values in Venus' thermosphere. Several factors may contribute to the mismatch between model and observations: (i) significant flux loss at limb points due to pointing/tracking errors, (ii) an oversimplified treatement of the observing geometry in the model and (iii) a spatially and temporally variable CO profile.

In principle, high signal-to-noise, high spectral resolution observations from an orbiting spacecraft could provide mapping data on the temperature field (and hence, if enough data are available, on the thermal wind field in Venus' thermosphere over 100–150 km. This would complement the dynamical information provided by the structure of the NO airglow at 115–150 km (Bougher et al. 1990). In spite of their lower spectral resolutions ($\approx$ 2000), the VIRTIS-H and PFS instruments aboard Venus Express are expected to detect the CO emissions in limb viewing, as did Galileo/NIMS during the 1990 flyby (Shirley et al. 1995). The spectral resolution should be sufficient for rotational temperature determinations, although the spatial coverage might be incomplete.

References

Alexander, M.J., Stewart, A.I.F., Solomon, S.C., Bougher, S.W., 1993. Local asymmetries in the Venus thermosphere. J. Geophys. Res. 98, 10849–10872.

Betz, A.L., Johnson, M.A., McLaren, R.A., Sutton, E.C., 1976. Heterodyne detection of CO_2 emission lines and wind velocity in the atmosphere of Venus. Astrophys. J. 208, L141–L144.

Billebaud, F., Crovisier, J., Lellouch, E., Encrenaz, T., Maillard, J.-P., 1991. High-resolution infrared spectrum of CO on Mars: evidence for emission lines. Planet. Space Sci. 39, 213–218.

Bougher, S.W., Borucki, W.J., 1994. Venus O_2 visible and IR nightglow: implications for lower thermosphere dynamics and chemistry. J. Geophys. Res. 99, 3759–3776.

Bougher, S.W., Dickinson, R.E., Ridley, C.E., Roble, R.G., 1988b. Venus mesosphere and thermosphere. III. Three–dimensional general circulation with coupled dynamics and composition. Icarus 73, 545–573.

Bougher, S.W., Gérard, J.C., Stewart, A.I.F., Fesen, C.G., 1990. The Venus nitric oxide night airglow: Calculations based on the Venus Thermospheric General Circulation Model. J. Geophys. Res. 95, 6271–6284.

Carlson, R.W., and 20 coauthors, 1991. Galileo infrared imaging spectroscopy measurements at Venus. Science 253, 1541–1548.

Chin, G., Weaver, H.A., 1984. Vibrational and rotational excitation of CO in comets. Astrophys. J. 284, 858–869.

Clancy, R.T., Muhleman, D.O., 1991. Long-term (1979–1990) changes in the thermal, dynamical, and compositional structure of the Venus mesosphere as inferred from microwave spectral lines observations of ^{12}CO, ^{13}CO, and C^{18}O. Icarus 89, 129–146.

Crisp, D., Meadows, V.S., Bézard., B., de Bergh, C., Maillard, J.-P., Mills, F.P., 1996. Ground-based near-infrared observations of the Venus night side: Near-infrared $O_2(^1\Delta)$ airglow from the upper atmosphere. J. Geophys. Res. 101, 4577–4593.

Crovisier, J., 1987. Rotational and vibrational synthetic spectra of linear parent molecules in comets. Astron. Astrophys. Suppl. Series 68, 223–258.

Crovisier, J., Encrenaz, T., 1983. Infrared fluorescence of molecules in comets: the general synthetic spectrum. Astron. Astrophys. 126, 170–182.

Crovisier, J., Le Bourlot, J., 1983. Infrared and microwave fluorescence of carbon monoxide in comets. Astron. Astrophys. 123, 61–66.

de Bergh, C., Crovisier, J., Lutz, B.L., Maillard, J.-P., 1988. Detection of CO infrared emission lines in spectra of Venus. Bull. Am. Astron. Soc. 20, 831.

Deming, D., Espernak, F., Jennings, D., Kostiuk, T., Mumma, M., Zipoy, D., 1983. Observations of the 10-μm natural laser emission from mesospheres of Mars and Venus. Icarus 55, 347–355.

Deming, D., Mumma, M.J., 1983. Modeling of the 10-μm natural laser emission from the mesospheres of Mars and Venus. Icarus 55, 356–368.

Diner, D.J., 1978. The equatorial and polar limb darkening of Venus in the 8–20 μm region. J. Atmos. Sci. 35, 2356–2361.

Durrance, S.T., 1981. The carbon monoxide fourth positive bands in the Venus dayglow 1. Synthetic spectra. J. Geophys. Res. 86(A11), 9115–9124.

Durrance, S.T., Barth, C.A., Stewart, A.I.F., 1980. Pioneer Venus observations of the Venus dayglow spectrum 1250–1430 Å, Geophys. Res. Letters 7, 222–224.

Encrenaz, T., Lellouch, E., Drossart, P., Feuchtgruber, H., Orton, G.S., Atreya, S.K., 2004. First detection of CO in Uranus. Astron. Astrophys. 413, L5–L9.

Farmer, C.B., Norton, C.H., 1989. A high-resolution atlas of the infrared spectrum of the Sun and the earth atmosphere from space. NASA Reference Publication 1224.

Gérard, J.C., Stewart, A.I.F., Bougher, S.W., 1981. The altitude distribution of the Venus ultraviolet nightglow and implications on vertical transport. Geophys. Res. Lett. 8, 633–636.

Goorvitch, D., Chackerian, C.Jr., 1994. Calculation of ^{12}C^{16}O and ^{13}C^{16}O $X^1\Sigma^+$ rovibrational intensities for $\nu \leq 20$ and $J \leq 150$. Astrophys. J. Suppl. 91, 483–489.

Hogerheijde, M.R., van der Tak, F.F.S., 2000. An accelerated Monte Carlo method to

solve two-dimensional radiative transfer and molecular excitation. Astron. Astrophys. 362, 697–710.

Huebner, W.F., Keady, J.J., Lyon, S.P., 1992. Solar photo rates for planetary atmospheres and atmospheric pollutants. Astrophys. Space Scie. 195, 1–294.

Inn, E.C.Y., Watanabe, K., Zelikoff, M., 1953. Absorption coefficients of gases in the vacuum ultraviolet. Part III. CO_2. J. Chem. Phys. 21, 1648–1650.

Johnson, M.A., Betz, A.L., McLaren, R.A., Sutton, E.C., Townes, C.H., 1976. Nonthermal !0 micron CO_2 emission lines in the atmospheres of Mars and Venus. Astrophys. J. 208, L145–L148.

Keating, G.M., Bertaux, J.L., Bougher, S.W., Cravens, T.E., Dickinson, R.E., Hedin, A.E., Nagy, A.F., Nicholson III, J.Y., Paxton, L.J., von Zahn, O., 1985. Models of Venus neutral upper atmosphere: structure and composition. Adv. Space Res. 5, 117–171.

Krasnopolsky, V.A., 1983. Venus spectroscopy in the 3000-8000 Å region by Veneras 9 and 10. In *Venus* , eds D.M. Hunten, L. Colin, T.M. Donahue and V.I. Moroz (Tucson: Univ. of Arizona Press), pp. 681–765.

Krishna Swamy, K.S., 1979. Intensities of the A–X and B–X bands of CO and CO^+ in comets. Astrophys. J. 227, 1082–1085.

Labs, D., Neckel, H. 1968. The radiation of the solar photosphere from 2000 Å to 100 μ. Z. Astrophys. 69, 1–73.

Lawrence, G.M., 1972. Photodissociation of CO_2 to produce CO($a^3\Pi$). J. Chem. Phys. 56, 3435–3442.

Lellouch, E., Goldstein, J.J., Rosenqvist, J., Bougher, S.W., Paubert, G., 1994. Global circulation, thermal structure and carbon monoxide distribution in Venus' mesosphere in 1991. Icarus 110, 315–339.

Lellouch, E., Clancy, T., Crisp, D., Kliore, A., Titov, D., Bougher, S.W., 1997. Monitoring of mesospheric structure and dynamics. In *Venus II*, eds S.W. Bougher, D.M. Hunten, and R.J. Phillips (Tucson: Univ. of Arizona Press), 295–324.

Lellouch, E., Coustenis, A., Sebag, B., Cuby, J.-G., López-Valverde, M., Schmitt, B., Fouchet, T., Crovisier, J., 2003. Titan's 5-μm window: observations with the Very Large Telescope. Icarus 162, 125–142.

Lewis, B.R., Carver, J.H., 1983. Temperature dependence of the carbon dioxide photoabsorption cross section between 1200 and 1970 Å. J. Quant. Spectrosc. Radiat. Transfer 30, 297–309.

López-Valverde, M.-A., Lellouch, E., Coustenis, A., 2005. Carbon monoxide fluorescence from Titan's atmosphere. Icarus 175, 503–521.

Maillard, J.-P., Lellouch, E., Crovisier, J., de Bergh, C., Bézard, B. 1995. Carbon monoxide 4.7 μm emission: a new dynamical probe of Venus' thermosphere. Bull. Amer. Astron. Soc. 27, 920.

Moroz, V., 1983. Stellar magnitude and albedo data of Venus. In *Venus* , eds D.M. Hunten, L. Colin, T.M. Donahue and V.I. Moroz (Tucson: Univ. of Arizona Press), pp. 27–35.

Mumma, M.J., DiSanti, M.A., Dello Russo, N., Fomenkova, M., Magee-Sauer, K., Kaminski, C.D., Xie, D.X. 1996. Detection of abundant ethane and methane, along with carbon monoxide and water in comet C/1996 B2 Hyakutake: Evidence for interstellar

origin. Science 272, 1310–1314.

Roldán, C., López-Valverde, M.A., López-Puertas, M., Edwards, D.P. 2000. Non-LTE infrared emissions of CO_2 in the atmosphere of Venus. Icarus 147, 11–25.

Roos, M., Drossart, P., Encrenaz, T., Lellouch, E., Bézard, B., Carlson, R.W., Baines, K.H., Kamp, L.W., Taylor, F.W., Collard, A.D., Calcutt, S.B., Pollack, J.B., Grinspoon, D.H., 1993. The upper clouds of Venus: determination of the scale height from NIMS-*Galileo* data. Planet. Space Sci. 41, 505–514.

Roos-Serote, M., Drossart, P., Encrenaz, T., Lellouch, E., Carlson, R.W., Baines, K.H., Taylor, F.W., Calcutt, S.B., 1995. The thermal structure and dynamics of the atmosphere of Venus between 70 and 90 km from the Galileo–NIMS spectra. Icarus 114, 300–309.

Seiff, A., 1983. Models of Venus' atmospheric structure, in *Venus*, eds D.M. Hunten, L. Colin, T.M. Donahue and V.I. Moroz (Tucson: Univ. of Arizona Press), pp. 1045–1048.

Shirley, J.H., Carlson, R.W., Kamp, L.W., Mehlman, R., 1995. Galileo NIMS observations of CO_2 and CO infrared resonance fluorescence from the Venus dayside. Bull. Amer. Astron. Soc. 27, 922.

Slanger, T.G., Cosby, P.C., Huestis, D.L., Bida, T.A., 2001. Discovery of the atomic oxygen green line in the Venus night airglow. Science 291, 463–465.

Starr, D.F., Hancock, J.K., 1975. Vibrational energy transfer in CO_2–CO mixtures from 163 to 406 K. J. Chem. Phys. 63, 4730–4734.

Stewart, A.I F., Gérard, J.C., Rusch, D.W., and Bougher, S.W., 1980. Morphology of the Venus ultraviolet night airglow. J. Geophys. Res. 85, 7861–7870.

Taylor, F.W., Beer, R., Chahine, M.T., Diner, D.J., Elson, L.S., Haskins, R.D., McCleese, D.J., Martonchik, J.V., Reichley, P.E., Bradley, S.P., Delderfield, J., Schofield, J.T., Farmer, C.B., Froidevaux, L., Leung, J., Coffey, M.T., Gille, J.C., 1980. Structure and meteorology of the middle atmosphere of Venus Infrared remote sensing from the Pioneer orbiter. J. Geophys. Res. 85, 7963–8006.

Taylor, F.W., Schofield, J.T., Valdes, P.J. 1985. Temperature structure and dynamics of the middle atmosphere of Venus. Adv. Space Res. 5, 5–23.

Welge K.H., Gilpin, R., 1971. Time-of-flight spectroscopy of CO_2 photodissociation in the vacuum ultraviolet. Electron emission from cesium surface by metastable singlet oxygen atoms. J. Chem. Phys. 54, 4224–4227.

Yung, Y.L., Delmore, W.B. 1982. Photochemistry of the stratosphere of Venus: implications for atmospheric evolution. Icarus 51, 199–247.

Zakharov, V., Biver, N., Bockelée-Morvan, D., Crovisier, J., Lecacheux, A., 2005. A radiative transfer simulation of water rotational excitation in comets. Bull. Amer. Astron. Soc. 37, 633–634.

Figures

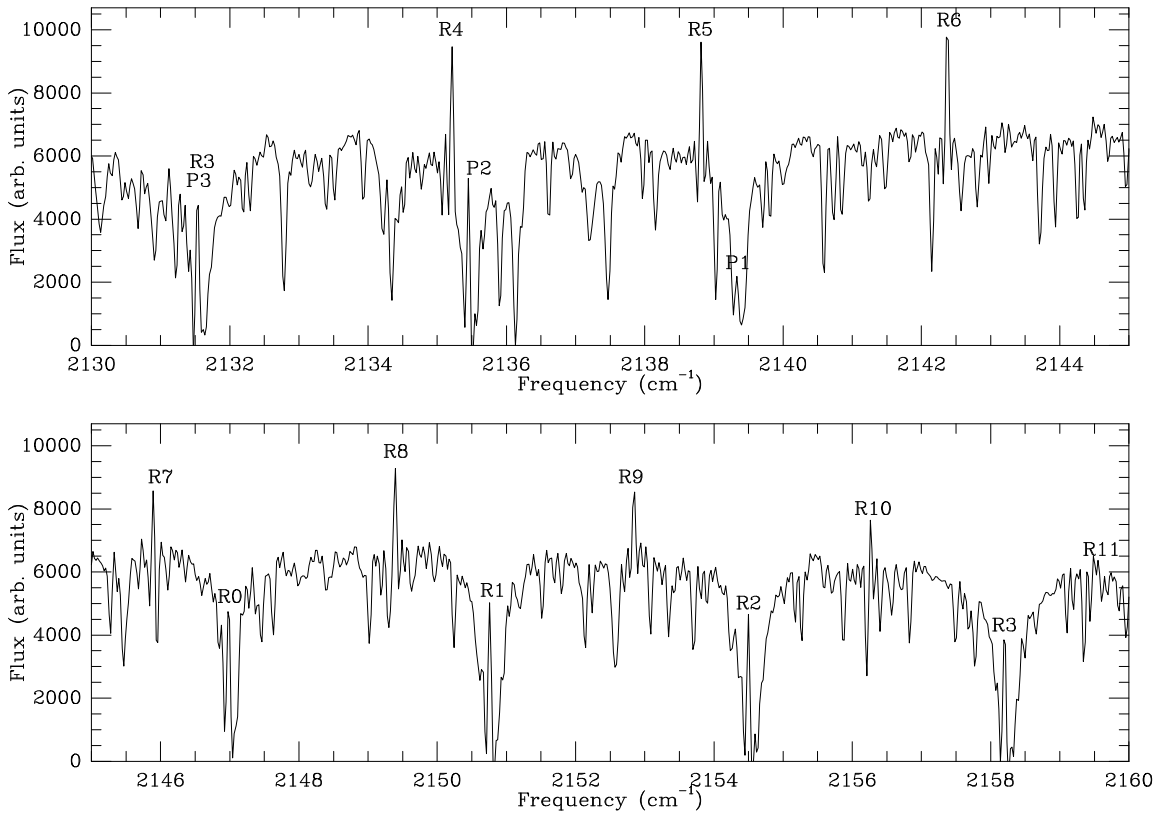

Figure 1: The Venus spectrum at 2130–2160 cm^{-1} observed on 10 January 1987 (uncorrected for telluric absorption and instrumental response). Emission lines of CO belonging to the v(1–0) band ($P\,1$ to $P\,3$ and $R\,0$ to $R\,3$) and (2–1) band ($R\,3$ to $R\,11$) are identified.

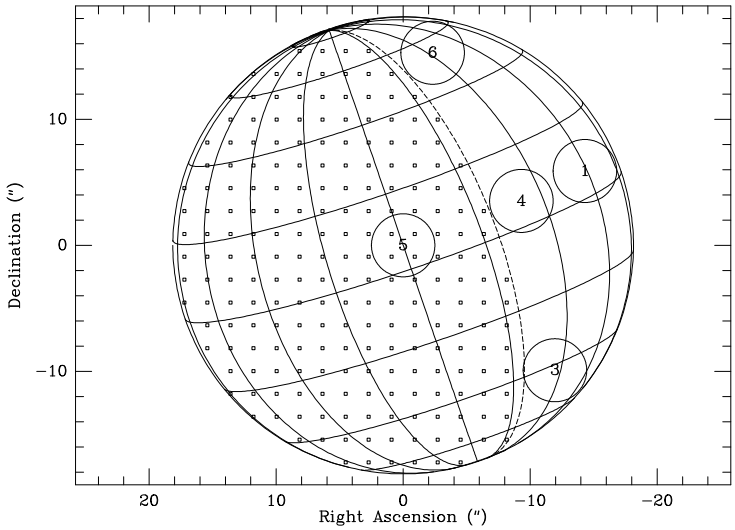

Figure 2: The geometry of the September 1994 observations. Venus is a 36″ disk whose evening (astronomical west) crescent is illuminated by the Sun. The dashed line indicates the terminator. The five target points with the 5″ aperture are indicated.

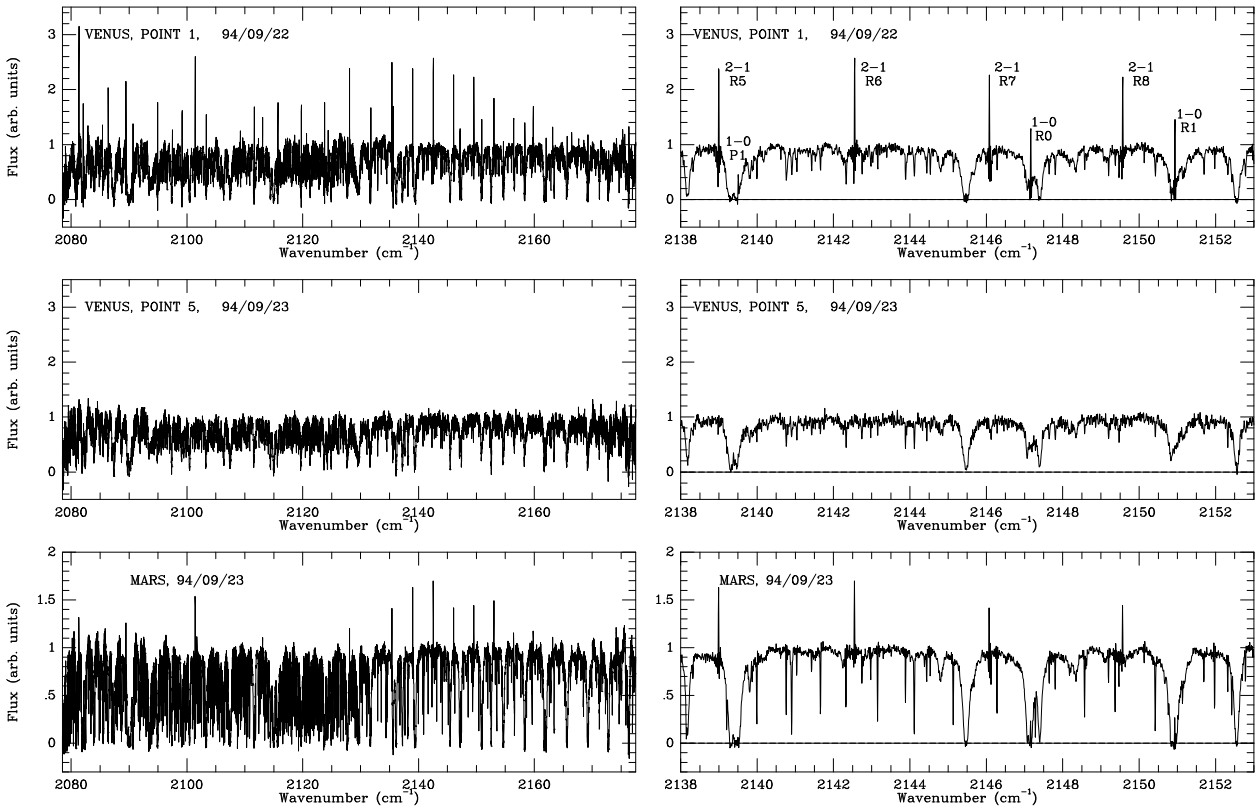

Figure 3: The overall structure of the CO v(2–1) and (1–0) emissions in the September 1994 observations. From top to bottom: a) Point 1 (equator of Venus, 3:40 pm). b) Point 5 (nightside of Venus). c) Mars. The full spectra are shown on the left, and enlargements of the 2138–2152 cm^{-1} region are shown on the right. The spectra are shown here before division by the Moon spectrum but after correction of the filter profile.

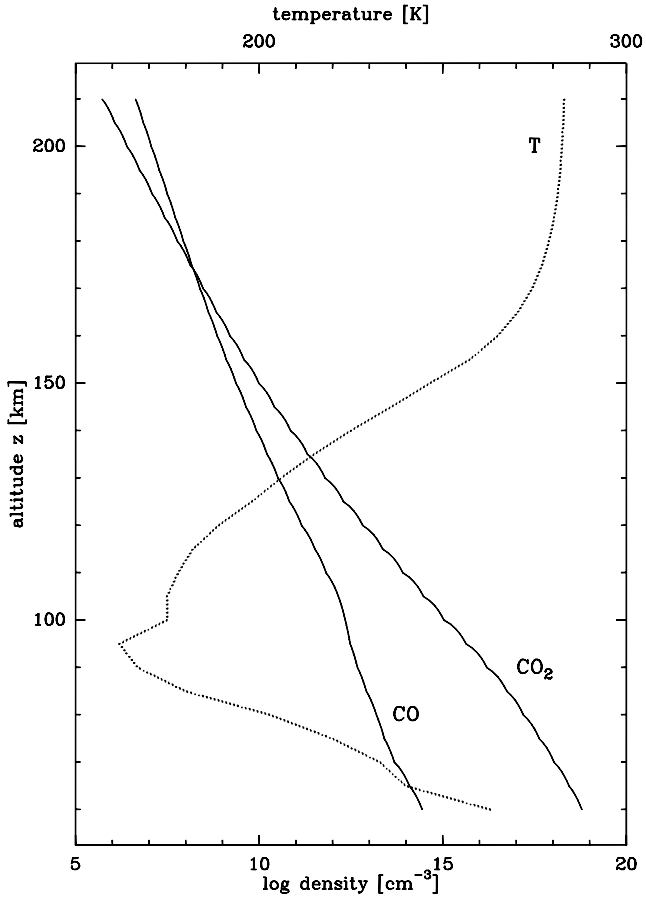

Figure 4: The CO and CO_2 density profiles and the temperature profile used in our model of the Venus atmosphere. They are taken from the VIRA model (Keating et al. 1985) at the subsolar point for altitudes $100 < z < 250$ km, and from Seiff (1983) for altitudes below 100 km (a slight modification was necessary to keep the CO profile continuous around 100 km).

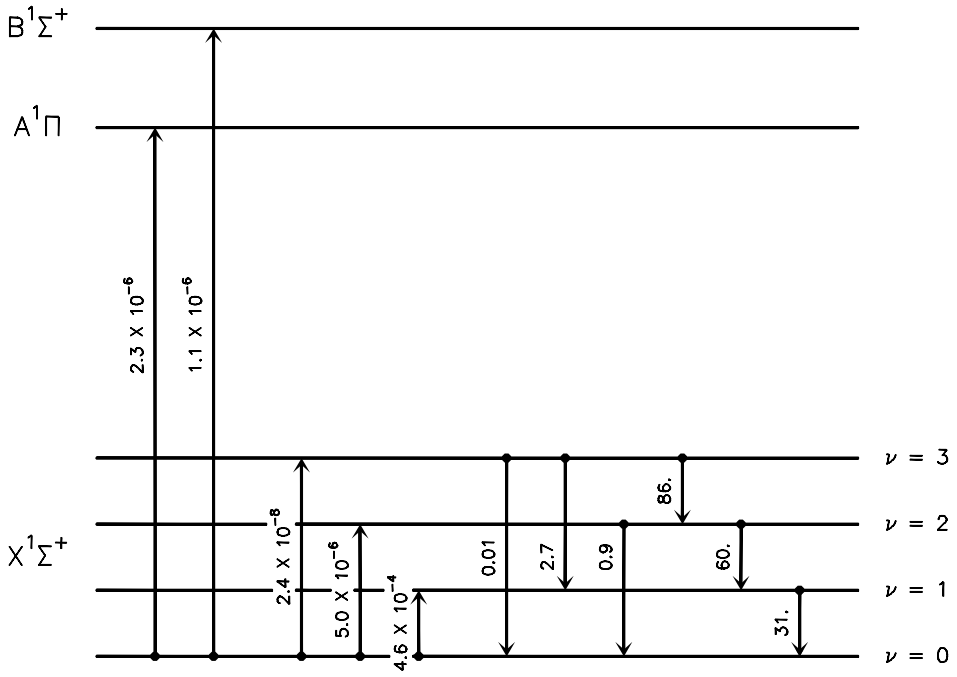

Figure 5: A schematic diagram (not to scale) of the electronic ground state first vibrational levels of CO and of its main electronic excited states. The excitation rates from the ground state, due to unattenuated solar radiation at the Venus distance, are indicated on the left. The Einstein coefficients for spontaneous emission of the various infrared bands are also given on the right. All units are in s^{-1}.

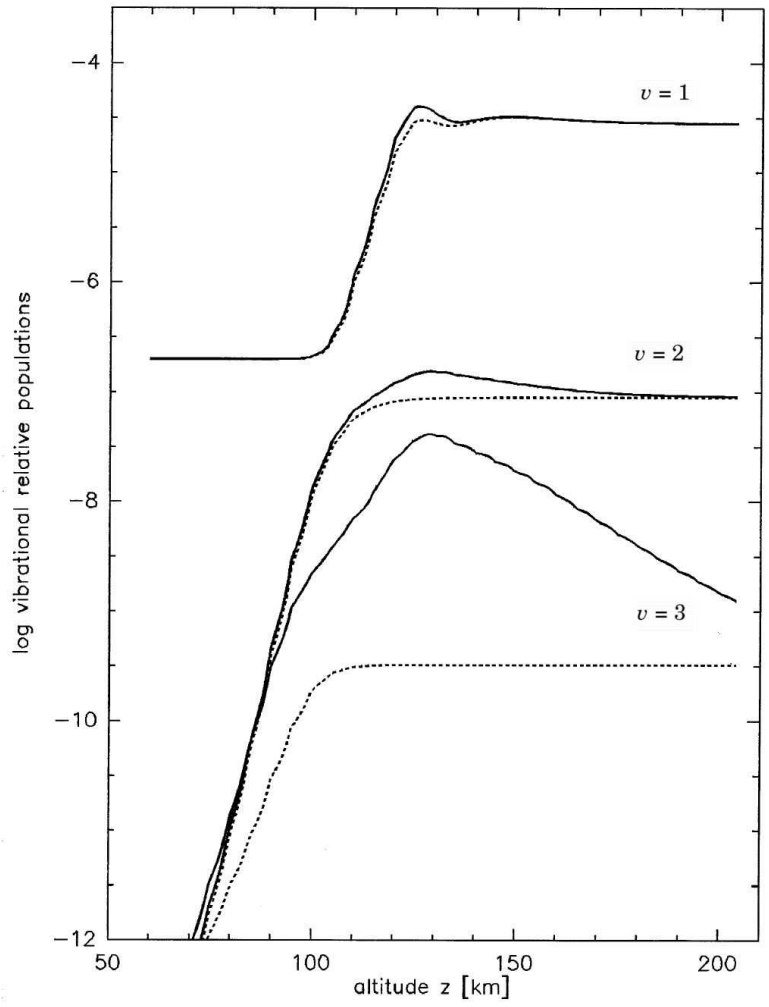

Figure 6: The relative populations of the vibrational levels of CO as a function of altitude, resulting from our model for Venus for a uniform temperature of 200 K. Full lines: nominal model; dashed lines: fluorescence only, neglecting CO_2 photolysis.

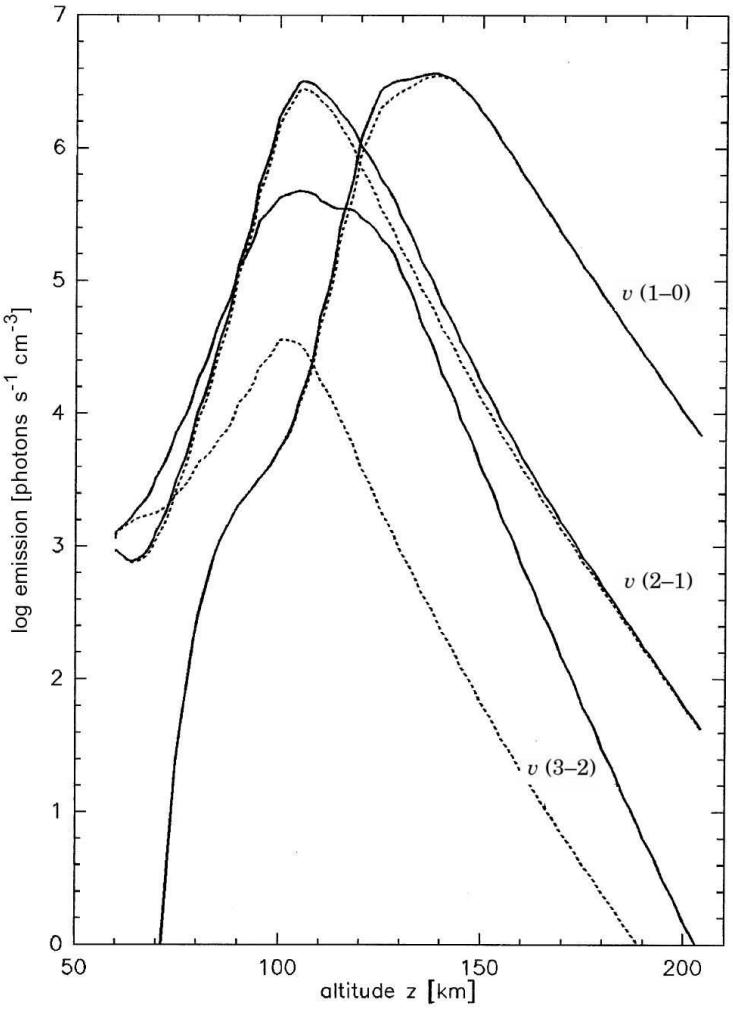

Figure 7: The volumic emission rates contributing to the emergent emissions, as a function of altitude, for the CO vibrational bands of the $\Delta v = -1$ sequence (sums of the individual ro-vibrational lines). This is given for our Venus model for a uniform temperature of 200 K. Full lines: nominal model; dashed lines: fluorescence only, neglecting CO_2 photolysis.

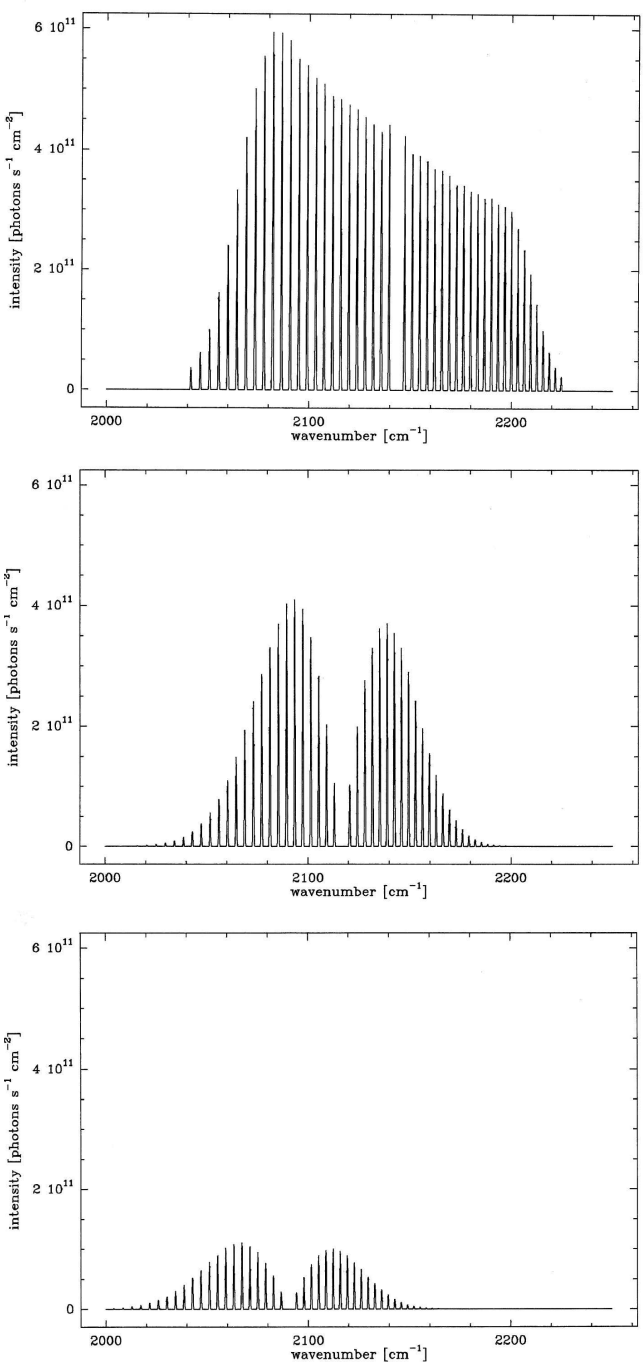

Figure 8: Rotational structure of the CO vibrational bands of the $\Delta v = -1$ sequence, resulting from our Venus model for a uniform temperature of 200 K. From top to bottom: $v = (1\text{–}0)$, $v = (2\text{–}1)$ and $v = (3\text{–}2)$ bands. Figs 5, 6 and 7 were computed for a solar zenithal angle $\Phi_s = 60°$ and an observer zenithal angle $\Phi_o = 45°$.

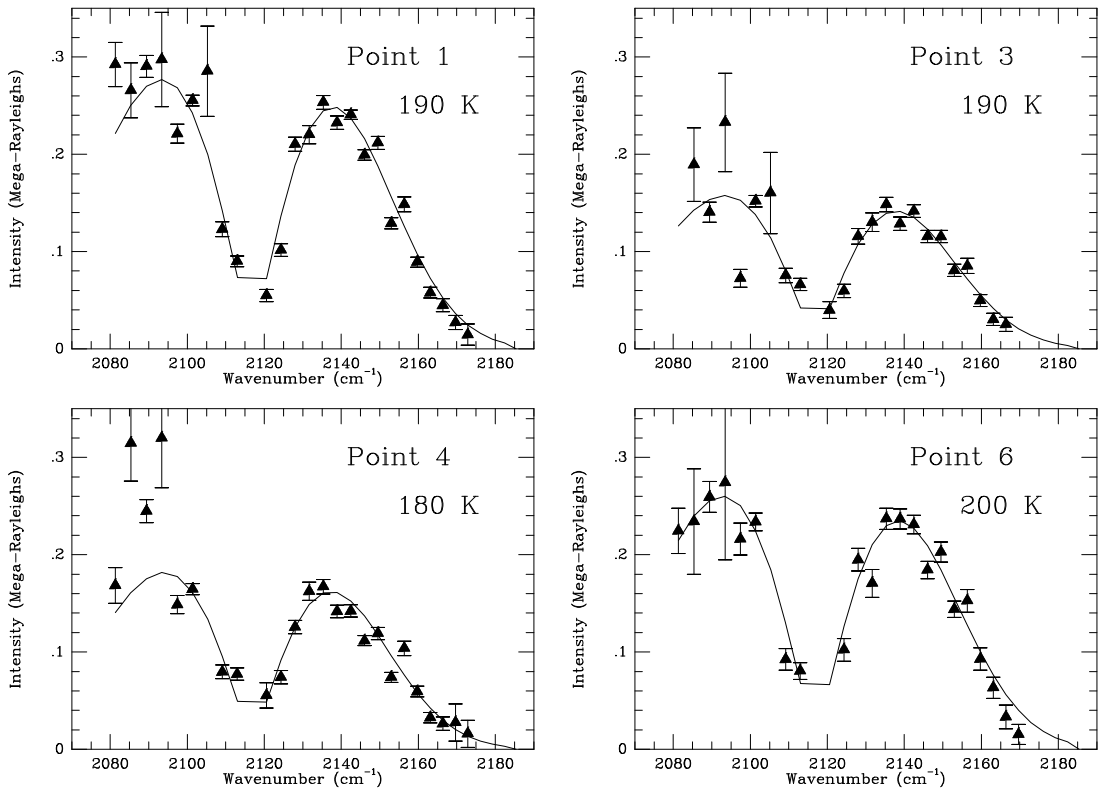

Figure 9: Intensity (in megarayleighs, or 10^{12} photons s^{-1} cm^{-2}) of the emission lines of the CO v(2–1) band for the various Venus points (September 1994 observations), with 1–σ error bars. Along are shown model fits calculated with the indicated rotational temperature and scaled by a constant multiplicative factor (see text).

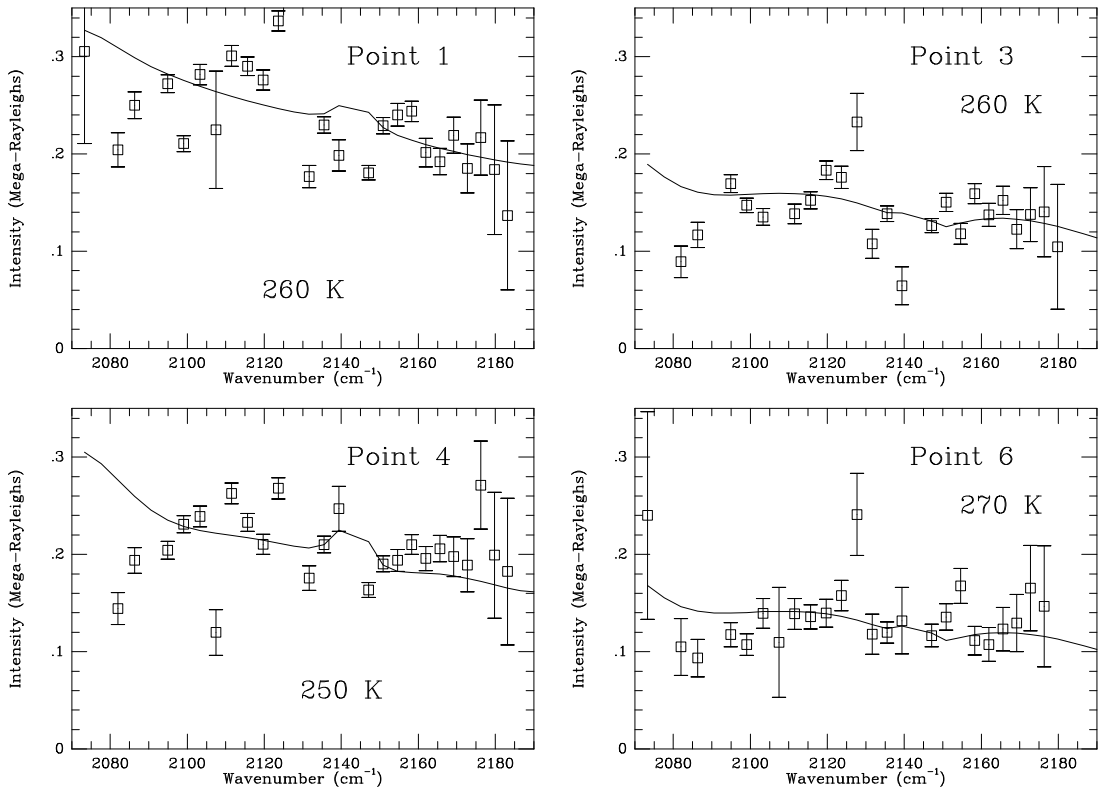

Figure 10: Same as Fig. 9 for the CO $v(1\text{–}0)$ band.

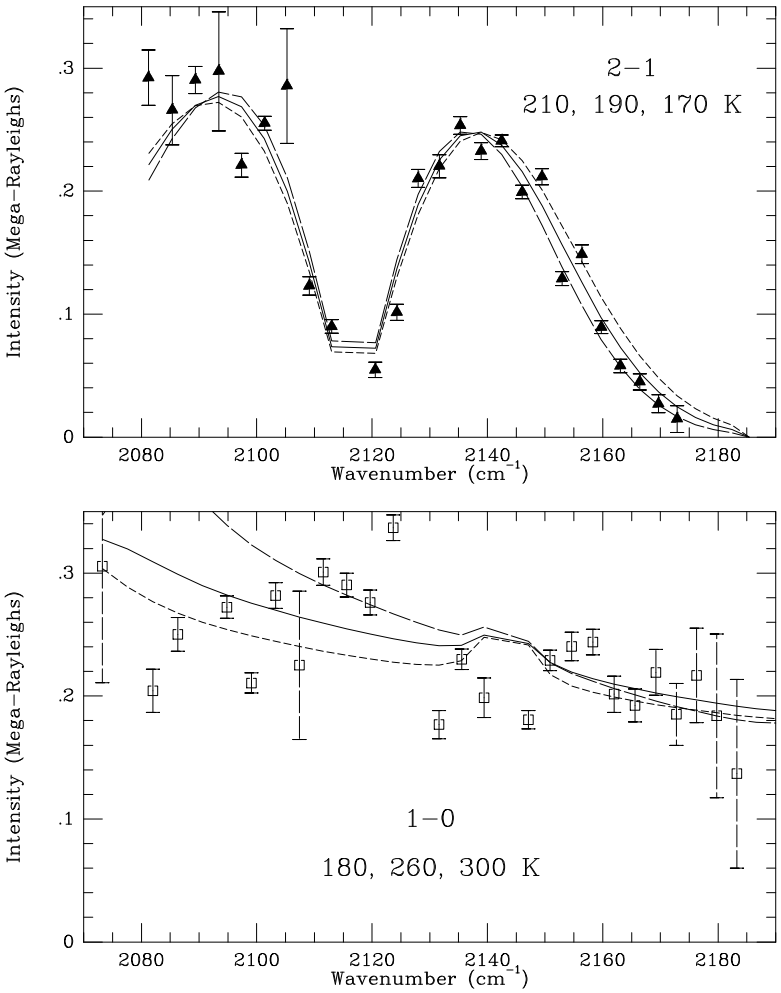

Figure 11: Intensity of the emission lines of the CO $v = (2–1)$ (top) and $v = (1–0)$ (bottom) bands at point 1 (September 1994 observations), with 1–σ error bars. Along are shown model fits calculated with several rotational temperatures and scaled by an adjustable multiplicative factor. Top panel — solid line: $T = 190$ K; short-dashed line: $T = 210$ K; long-dashed line: $T = 170$ K. Bottom panel — solid line: $T = 260$ K; short-dashed line: $T = 300$ K; long-dashed line: $T = 180$ K.